

Journal of Materials Chemistry A

Accepted Manuscript



This is an *Accepted Manuscript*, which has been through the Royal Society of Chemistry peer review process and has been accepted for publication.

Accepted Manuscripts are published online shortly after acceptance, before technical editing, formatting and proof reading. Using this free service, authors can make their results available to the community, in citable form, before we publish the edited article. We will replace this *Accepted Manuscript* with the edited and formatted *Advance Article* as soon as it is available.

You can find more information about *Accepted Manuscripts* in the [Information for Authors](#).

Please note that technical editing may introduce minor changes to the text and/or graphics, which may alter content. The journal's standard [Terms & Conditions](#) and the [Ethical guidelines](#) still apply. In no event shall the Royal Society of Chemistry be held responsible for any errors or omissions in this *Accepted Manuscript* or any consequences arising from the use of any information it contains.

ARTICLE

Multi-shelled hollow carbon nanospheres for lithium-sulfur batteries with superior performances

Cite this: DOI: 10.1039/x0xx00000x

Shuangqiang Chen, Xiaodan Huang, Bing Sun, Jinqiang Zhang, Hao Liu, Guoxiu Wang*

Received
Accepted

DOI: 10.1039/x0xx00000x

www.rsc.org/

Abstract. Lithium-sulfur batteries are regarded as a promising energy storage system. However, it is plagued by fast capacity decay, low Coulombic efficiency, severe shuttle effect and low sulfur loading in cathodes. To address these problems, effective carriers are highly demanded to encapsulate sulfur and extend cycle life. Herein, we report an aqueous emulsion approach and *in-situ* sulfur impregnation to synthesize multi-shelled hollow carbon nanospheres encapsulated sulfur composites with a high percentage of sulfur loading (86 wt.%). When applied as cathodes in lithium-sulfur batteries, the composite materials delivered a high specific capacity of 1350 mAh/g and excellent capacity retention (92% for 200 cycles). Further measurements at high current densities also demonstrate significantly enhanced cyclabilities and high rate capabilities.

Introduction

Energy storage devices with merits of high energy density, long cycle life, low cost and safety are in high demand. Substantial efforts have been devoted to develop various energy storage systems, including traditional secondary batteries, lithium-ion, lithium-oxygen and lithium-sulfur (Li-S) batteries, for both portable electronic devices and electric vehicles or plug-in hybrid electric vehicles.¹⁻⁹ Among them, Li-S batteries are regarded as a promising system with many advantages, such as low cost, natural abundance of sulfur (around 3% of earth mass), environmental friendliness and high theoretical capacity (1673 mAh/g, energy density of ~2600 Wh/kg).^{2, 10-13} Previous reports on sulfur loading in cathodes are mostly around 70%, which is confined by volume expansion (~80%, charge) and limited inner voids. Most importantly, recent report by Abruña group showed that the volumetric energy density of Li-S cells with a sulfur loading more than 70 wt. % exceeded that of lithium ion cells.¹⁴ In order to achieve high energy density, high percentage of sulfur loading carriers with sufficient inner spaces and good conductivity are required to develop high performance Li-S batteries. In the discharge process of a Li-S battery, there are two main reaction stages, and each stage includes several reactions relating to the transformation of cyclo-octasulfur (S₈) to soluble long-chain lithium polysulfides at the first plateau (2.15-2.4 V), and further decompose to insoluble lithium sulfide (Li₂S) or lithium persulfide (Li₂S₂) at the second plateau (2.0-2.1 V). The subsequent charging process is mainly dominated by the slow kinetic reaction of

oxidizing lithium sulfides to lithium polysulfides, and then rapid reversing to cyclo-octasulfur.¹⁵⁻¹⁷ Two broad oxidation peaks were commonly observed in previous reports.¹⁶⁻¹⁸

Despite many advantages, the practical application of Li-S batteries is hindered by rapid capacity decay. This is caused by many reasons, including the insulating nature of sulfur, dissolution of lithium polysulfide ions (causing shuttle effect), large volume changes and the formation of lithium dendrite.¹⁹⁻²³ Furthermore, insoluble Li₂S₂ and Li₂S of the discharged products tend to precipitate on the surface of electrodes.²⁴ Conducting additives or graphitized carbon matrices were employed to improve the conductivity and to confine polysulfides dissolution.^{10, 21, 25-30} Various hollow (nanospheres^{21, 31-33}), flexible (carbon paper³⁴ and graphene^{18, 35-37}) or tunnel carbon materials (carbon nanotube,³⁸⁻⁴⁰ carbon nanofibers^{20, 41} and highly ordered porous carbon matrix^{12, 42}) were also used to encapsulate sulfur and confine the shuttle effect originated from soluble lithium polysulfides, which is considered as the physical confinement. Conducting polymers and amphiphilic polymers, including poly (3,4-ethylenedioxythiophene) (PEDOT),⁴³ polypyrrole (PPY),⁴⁴ polyethylene glycol (PEG),^{12, 27} polyaniline (PANI)⁴⁵ and polyvinylpyrrolidone (PVP)^{41, 46} have also been applied to restrain the dissolution of polysulfides ions through chemical interactions, which can be regarded as a chemical confining strategy.⁴⁷⁻⁵¹ Moreover, the addition of LiNO₃ in electrolyte also suppresses the shuttle effect.⁴¹ Combining the physical and chemical approaches as a dual sulfur confining tactic would open new opportunities to rationally develop cathode materials

with superior properties. However, to date, only a few reports discuss the dual sulfur confining strategy.^{12,17}

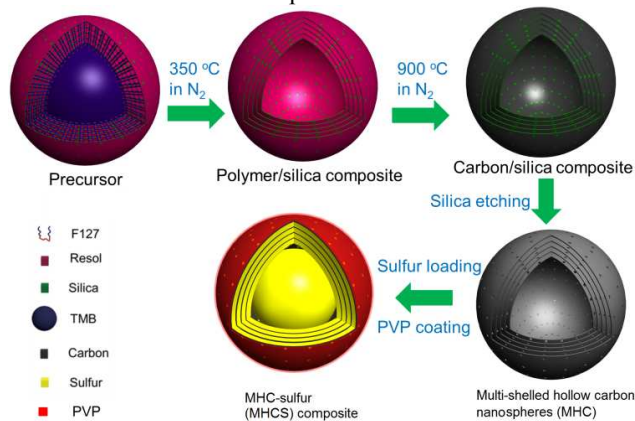
Besides the improvements on electrode conductivity and the confinements on shuttle effect, modification on sulfur composites and newly designed sulfur components have demonstrated enhanced electrochemical performances. Cui *et al.* prepared hollow sulfur nanospheres with the conductive polymer PEDOT coating, which achieved an initial capacity of 1267 mAh/g at 0.2C, with a capacity retention ratio of 74% after 100 cycles, and a reversible capacity of 739 mAh/g even after 300 cycles.⁴⁵ Long *et al.* reported a sustainable and efficient way of layer-by-layer catalyzing and depositing sulfur on a nitrogen-contained mesoporous carbon framework, demonstrating a high reversible capacity of 939 mAh/g after 100 cycles at 0.2C, and an excellent rate capability of 527 mAh/g up to 5C.⁴² Cheng *et al.* developed a graphene-pure-sulfur sandwich structure by clamping pure sulfur between two well-prepared graphene membranes, and assembled with a commercial separator pre-coated with another graphene membrane, showing a resumed capacity of 950 mAh/g, with a capacity retention ratio of 90.3% after 100 cycles at a current density of 0.75 A/g.³⁶ Liu *et al.* designed a hybrid anode with electrically connected graphite and lithium foil to control side-reactions on the surface of lithium foil, achieving a high capacity of 800 mAh/g for 400 cycles at a high current density of 1,737 mA/g, with a high Coulombic efficiency.⁵²

Multi-shelled carbon and metal oxides nanospheres with high surface area, high electron mobility and robust physical architecture have been extensively applied in lithium ion batteries and photovoltaic cells, exhibiting superior electrochemical and catalytic performances.⁵³⁻⁶⁰ Similarly, multi-shelled hollow carbon nanospheres (MHC) with high specific surface area and large total pore volume could be an ideal carrier for sulfur immobilization.⁶¹ Voids between carbon layers can provide a huge space to accommodate sulfur and tolerate the volume change during charge/discharge processes;⁶²⁻⁶⁷ While the multi-shelled hollow carbon skeletons can enhance the electrode conductivity and prevent sulfur loss. Compared with mono-shelled and double-shelled carbon nanospheres,³¹ the multi-shelled spherical structure may offer extra protection to sulfur, because multiple carbon shells can provide alternating barriers to restrain the dissolution of polysulfides.

Herein, we report the synthesis of multi-shelled hollow carbon nanospheres encapsulated sulfur (MHCS) composites as sulfur-rich cathode materials for high performance Li-S batteries. MHC with a high specific surface area of 1050 m²/g was prepared by an aqueous emulsion approach. Through an *in-situ* sulfur impregnation, MHCS composites with the highest sulfur loading of 86 wt. % were achieved. When applied as cathodes in lithium sulfur batteries, the composites delivered a high specific capacity of 1350 mAh/g at the current density of 0.1C (167.3 mA/g). The composites also exhibited significantly enhanced cycling stability and high rate capabilities.

Results and discussion

The schematic illustration of the synthesis procedure is presented in Scheme 1. Multi-shelled hollow carbon nanospheres were synthesised by an aqueous emulsion approach, during which 1, 3, 5-trimethylbenzene (TMB) served as an organic co-solvent, and silica and Pluronic F127 served as co-templates.⁶¹ After heat treatment at high temperature in an inert atmosphere and the subsequent removal of silica, multi-shelled hollow carbon nanospheres were obtained.



Scheme 1. Schematic illustration of the synthesis of MHCS composites.

Figures 1a and 1b show the low and high magnification field emission scanning electron microscopy (FESEM) images of multi-shelled hollow carbon nanospheres. Homogenous multi-shelled hollow carbon nanospheres with a diameter of approximately 150 nm are presented. Figure 1c exhibits the transmission electron microscopy (TEM) image of multi-shelled hollow carbon nanospheres. The multi-shelled hollow structure of MHC with a shell thickness of 20 nm is shown in Figure 1d. A six layer-lamellar structure can be clearly identified. The interlayer distance is approximate 3 nm, which provides large inner spaces to accommodate guest components. Additionally, many tiny pillars can be distinguished in interlayer spaces. Nitrogen adsorption-desorption results presented in Figure S1 (Supplementary information) exhibit the changes of structural features of products obtained at each stage. Before removal of the silica template, the interlayer spaces and inner voids are partially occupied. Once the silica template is etched by a strong base aqueous solution, the surface area of multi-shelled hollow carbon nanospheres dramatically increases. The Brunauer-Emmett-Teller (BET) surface areas calculated from Figures S1a₁ and S1b₁, rapidly increase from 226 m²/g to 1050 m²/g, verifying that vast mesoporous voids are released. The corresponding pore size distributions in Figures S1a₂ and S1b₂ also provide additional evidence to demonstrate the changes. Before etching, the average pore size appears at around 8 nm, which is associated with the pyrolysis of triblock copolymers (F127). Subsequently, after the high temperature treatment and removal of silica, two

more peaks of pore sizes appear at around 4.5 nm and 50 nm, respectively. This indicates that the additional spaces previously occupied by silica are released and some mesopores are probably formed during the etching process.⁴⁴ Estimated from the isotherms in Figure S1b₂ (Supplementary information), MHC material has a high total pore volume of 0.75 cm³/g.

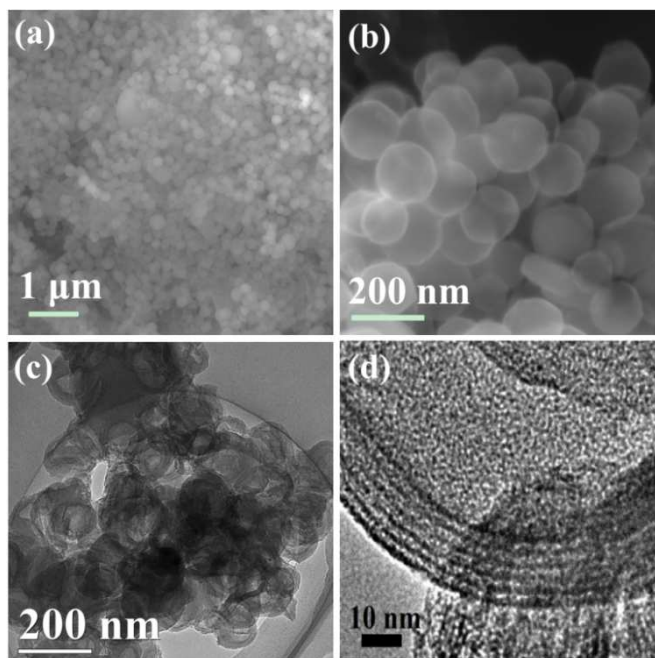
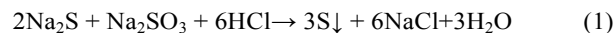


Figure 1. Morphology observation and structural characterization of MHC. (a-b) Low and high magnification FESEM images of MHC. (c) TEM image of MHC. (d) HRTEM image of MHC.

The impregnation of sulfur was performed by an *in-situ* approach and then coated by polyvinyl pyrrolidone (PVP). Sulfur impregnation proceeded *via* a disproportionate reaction, which can be described in a chemical equation as:



After further heat treatment, sulfur was absorbed into the mesopores and stored in the interlayer spaces and hollow carbon cavities *via* the strong capillary forces. MHCS composites with uniform sizes and homogeneous spherical morphology are shown in Figure 2a. For comparison, the morphology of pure sulfur is presented in Figure S2a-b (Supplementary information), displaying a micro-sized irregular granular structural feature. A high magnification view of MHCS composites is presented in Figure 2b. Compared with the semi-transparent pristine MHC (Figure 1a), MHCS composites exhibit a much deeper contrast, suggesting a successful S encapsulation. The insert image in Figure 2b shows the relatively dense nature of the sample, implying the

existence of sulfur. No obvious sulfur aggregates can be found in either Figure 2a or 2b, which indicates a very homogeneous impregnation of sulfur. The TEM image of MHCS composites is shown in Figure 2c, and the insert image in Figure 2c also exhibits a darker contrast than the pure carbon nanospheres (Figure 1b), indicating a good sulfur loading. Yet, the spherical morphology is still maintained. The elemental mapping image in Figure 2d further reveals the distribution of sulfur (red) and carbon (green) elements in MHCS composites. Apparently, sulfur is distributed in carbon interlayer voids and hollow carbon cavities. The insert images in Figure 2d are the corresponding elemental mapping in TEM. It is worth to note that sulfur (red) with a tiny size of around 5 nm is distributed in the inter-shelled carbon nanostructure (green). Sulfur is preferred to be accommodated in the inter-shelled spaces other than the large hollow chamber through the strong attraction forces between sulfur and multilayered lamellar carbon structure. Pure sulfur rarely can be observed outside of multi-shelled hollow carbon nanospheres. More FESEM and TEM images, elemental mapping images and their corresponding energy dispersive X-ray (EDX) spectrum are presented in Figure S3a-d and Figure S4a-d (Supplementary information). To further confirm the homogeneous sulfur impregnation. It should be noted that those multi-shelled hollow carbon nanospheres are completely filled by sulfur, but some of them have only their interlayer voids filled, implying that the encapsulation process is started from voids on the shell, then diffused inward, layer by layer, finally reaching hollow centers. Nitrogen adsorption-desorption results also reveal the internal structure change after sulfur impregnation. Both the specific surface area and the amount of mesopores are substantially decreased. Sulfur is homogeneously distributed in the carbon nanospheres and occupies the mesopores, which reduces the surface area to 182 m²/g (base on Figure S1c₁, supplementary information), and pore volume also decrease from 0.75 cm³/g of MHC to 0.16 cm³/g of MHCS composites. There is no apparent peak in the pore size distribution plot in Figure S1c₂ (Supplementary information), implying that the mesopores are completely occupied by sulfur.

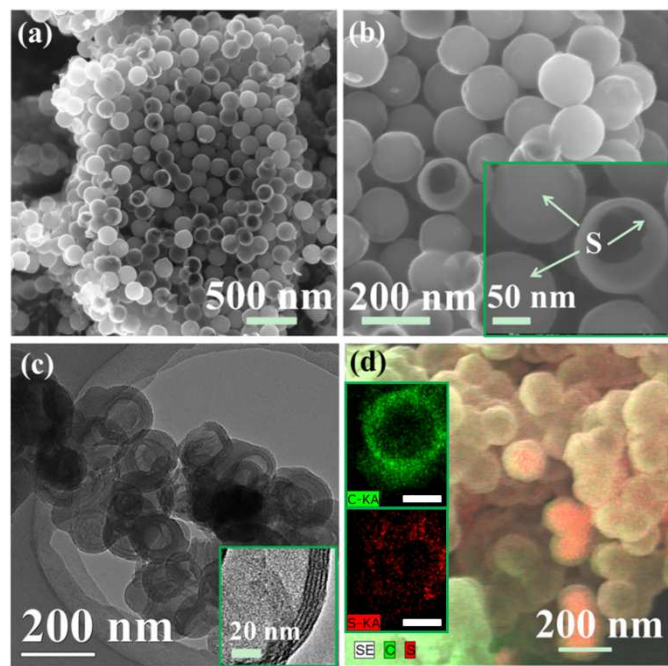


Figure 2. (a) Low magnification FESEM image of MHCS composites. (b) High magnification FESEM image of MHCS composites with an insert image of an enlarged view. (c) TEM image of MHCS composites. The inset is a HRTEM image of MHCS composites. (d) Elemental mapping SEM images of sulfur (red) and carbon (green) in MHCS composites. The insets are TEM elemental mapping of carbon (green) and sulfur (red). The scale bar is 100 nm.

MHC, pure S and MHCS were characterized by X-ray diffraction (XRD) to reveal the crystalline nature of the samples (Figure S5a). The observation of the (002) peak in the pattern of MHC implies carbon nanospheres are partially graphitized during the high temperature calcination. The XRD pattern of MHCS composites can be distinguished as the characteristic peaks of crystalline sulfur, which agrees well with those peaks of pure sulfur (indexed to JCPDS NO. 42-1278). The Raman spectrum intensity ratio of I_D/I_G for multi-shelled hollow carbon nanospheres equals the 1.43 in Figure S5b (Supplementary information), further proving the partial graphitization of carbon at high temperature, which should benefit for the enhancement of the electrical conductivity. Compared with the Raman spectrum of pure sulfur, the intensities of peaks at 205 and 485 cm^{-1} of MHCS composites substantially decrease, implying that the signal of sulfur is occluded by multi-shelled hollow carbon nanospheres, and that less sulfur can be detected on the outside of MHC.

The loading amount of sulfur in those multi-shelled hollow carbon nanospheres has been determined to be 86 wt. % by thermal gravimetric analysis (TGA) in Figure 3, which is the highest sulfur content to our best knowledge. It is worth noting that the evaporating temperature of sulfur accommodated in MHC is around 250 $^{\circ}\text{C}$, which is higher than that of pure sulfur (180 $^{\circ}\text{C}$). This might be ascribed to a strong affinity between sulfur and multi-shelled hollow carbon nanospheres,

demonstrating enhanced thermal stability of MHCS composites. The corresponding differential scanning calorimetry (DSC) plot of MHCS composites is also presented in Figure 3. The first peak positioned at around 250 $^{\circ}\text{C}$ is ascribed to the evaporation of sulfur stored in the carbon interlayers, and the second peak at 320 $^{\circ}\text{C}$ might be related to sulfur absorbed in the carbon inner cores. This retardation phenomenon demonstrates the strong physical confinement of multi-shelled hollow carbon nanospheres for sulfur. The peak at 600 $^{\circ}\text{C}$ is related to the pyrolysis of MHC.

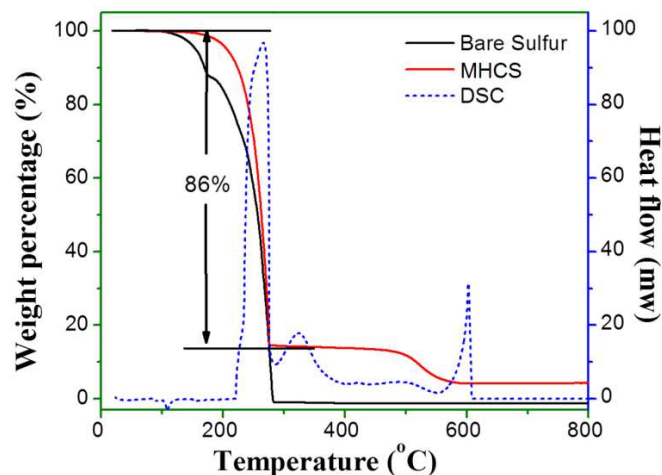
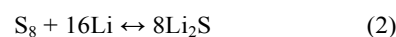


Figure 3. Thermogravimetric analysis of pure sulfur and MHCS composites (The dashed line is the corresponding differential scanning calorimetry of MHCS composites).

The electrochemical performances of MHCS composite were systematically measured by cyclic voltammogram (CV), galvanostatic charge/discharge cycling tests and electrochemical impedance spectroscopy (EIS). The CV curves in Figure 4a illustrate the typical electrochemical reaction behaviors between Li^+ ions and sulfur in the multi-shelled hollow carbon nanosphere-sulfur composite. Two broad reduction peaks centered at 2.28 V and 2.05 V were observed, corresponding to the two main stages of reduction reactions.^{48, 49, 51-53} The first peak is ascribed to the transformation of cyclo-octasulfur to soluble long chain lithium polysulfides, related to a fast kinetic reaction; While the other one originates from further decomposition of those polysulfides to insoluble $\text{Li}_2\text{S}_2/\text{Li}_2\text{S}$, corresponding to the slow kinetics.⁶⁵ One main peak associated with slow oxidation kinetics from lithium sulfides to lithium polysulfides and cyclo-octasulfur dominates the subsequent electrochemical reaction. The corresponding electrochemical reaction equation can be described as:



Apparently, little peak changes demonstrate the good reversibility and successful suppression of shuttle effect in the sulfur nanocomposites. The reduction peak position slowly shifted to lower voltage, which is ascribed to the diffusion

controlled chemical polarization. Furthermore, the perfect flat anodic base lines suggest that the shuttle effect at cathode has been almost eradicated.

Typical charge/discharge profiles in the first and 200th cycle recorded at the current density of 0.1C (167.3 mA/g) are presented in Figure 4b, in the voltage range of 1.7-2.6 V. A high initial discharge specific capacity of the MHCS electrode delivered 1350 mAh/g. Two main characteristic plateaus corresponding to the formation of long-chain polysulfides at around 2.28 V and short-chain $\text{Li}_2\text{S}_2/\text{Li}_2\text{S}$ centered at 2.1V are observed, which agrees well with the electrochemical behaviors in CV curves. After 200 cycles, a reversible capacity of 1250 mAh/g (1075 mAh/g based on the entire electrode mass) is well maintained with a capacity retention ratio of 92%,

demonstrating an excellent cycling stability. However, without the confinement of multi-shelled hollow carbon nanospheres, the pure sulfur electrode is plagued by an insulation nature and the severe shuttle effect of lithium polysulfides. It exhibits a charge capacity of 1203 mAh/g with a reversible capacity of 801 mAh/g and a low Coulombic efficiency of 33.4% in the 1st cycle (Figure S6a, supplementary information). The cycling performances of the MHCS electrode and the pure sulfur electrode are shown in Figure 4c, with insert plots of the corresponding Coulombic efficiencies. A significantly improved long-term stability of the MHCS electrode has been achieved, implying the excellent sulfur confining effect of multi-shelled hollow carbon nanospheres.

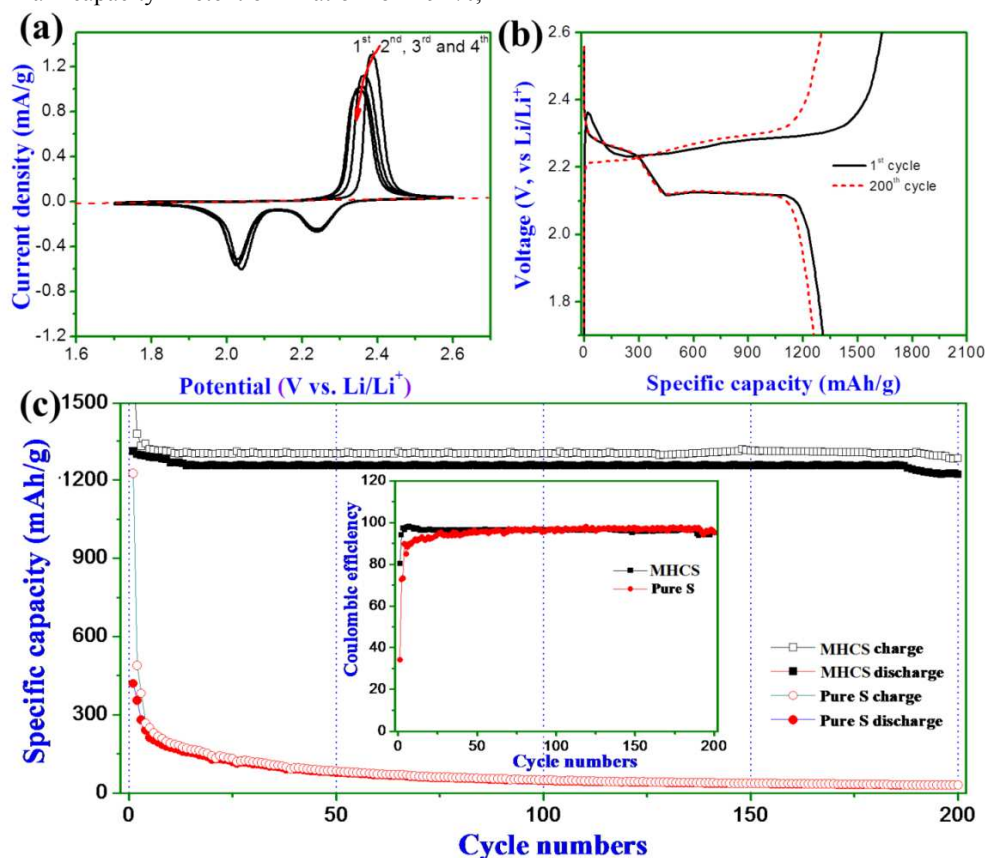


Figure 4. Electrochemical performances of pure sulfur and MHCS. (a) Cyclic voltammogram of MHCS composite at a scan rate of 0.1 mV/s. (b) The charge/discharge profiles of MHCS composites in the 1st and 200th cycles. (c) The cycling performances of pure sulfur and MHCS composites. The insert shows the corresponding Coulombic efficiency of the two materials.

Aiming to examine the cycling performances of MHCS electrodes at high current densities, the electrodes were cycled at several current rates (0.5C, 1C and 5C), and the results are shown in Figure 5. Figure 5a shows the cycling performances under the step-wise current rate tests, exhibiting the stable cyclability at high current rates, and the complete capacity recovery (back to 0.1C). The associated charge/discharge profiles at different current rates are shown in Figure S6b (Supplementary information). Discharge plateaus become shortened and lower when the current densities are increased, which is probably ascribed to the conductivity limitation of the

sulfur electrode, the fast lithium ion diffusion and subsequent electrode polarization.

Long-term cycling performances of MHCS cathodes at different current rates are presented in Figure 5b. The MHCS electrode exhibits an initial specific capacity of 1057 mAh/g at 0.5C (909 mAh/g based on entire electrode mass), with a capacity retention ratio of 94% after 200 cycles. The electrode delivered 1003 mAh/g (862 mAh/g based on entire electrode mass) and 541 mAh/g (465 mAh/g based on entire electrode mass) at 1C and 5C in the initial cycle, respectively. After 200 cycles, specific capacities of MHCS composites still maintain

at 846 mAh/g and 452 mAh/g, with capacity retention ratios of 84% and 83.5%, respectively. However, without the PVP polymer coating, the cycling performance of sulfur cathode at

1C rate exhibits a capacity fade tendency (as shown in Figure S6c). The capacity retention ratio is only 53.9%.

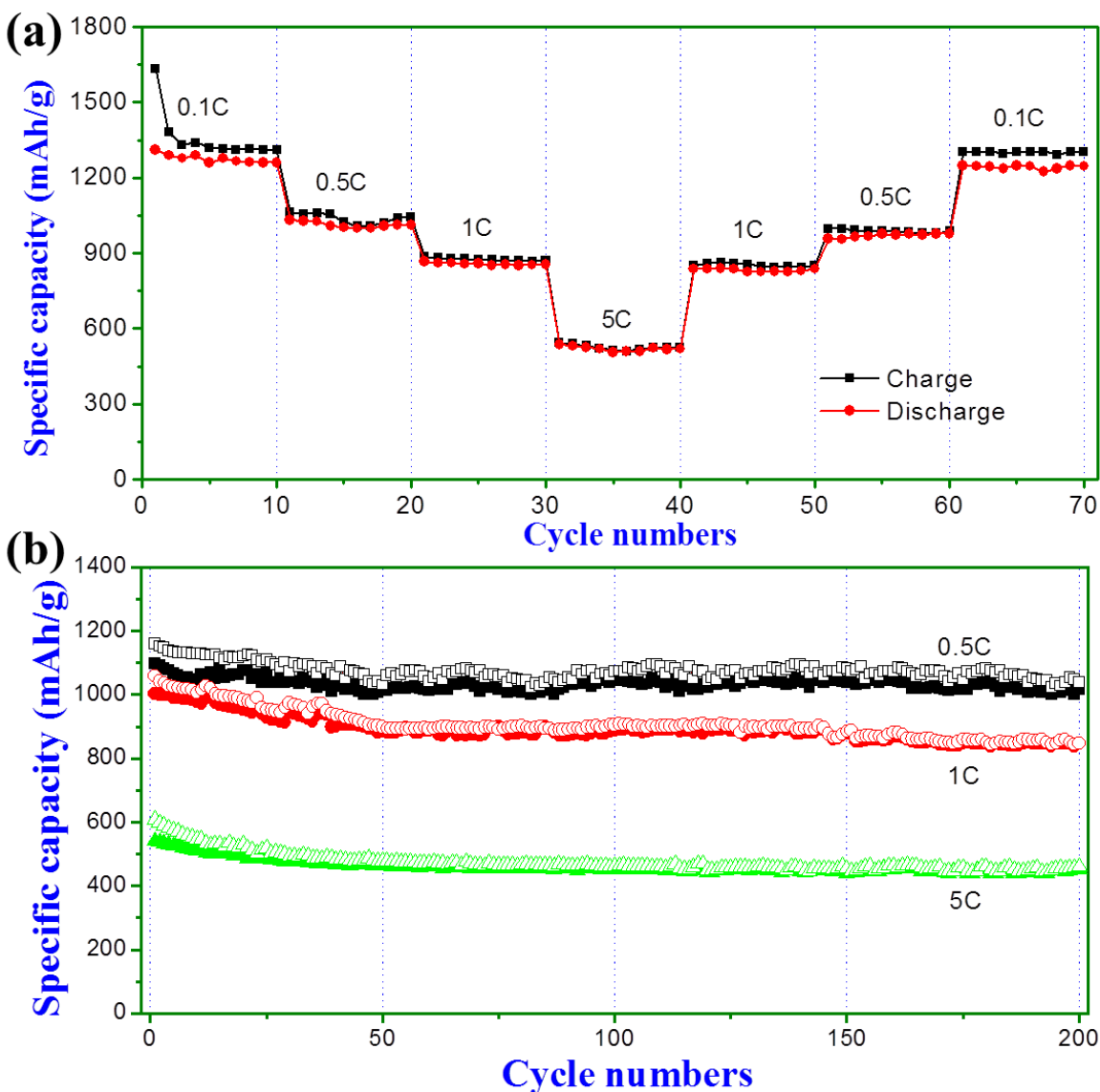


Figure 5. Electrochemical performances of MHCS composites at different current densities. (a) Step-wise cycling performance of MHCS composites. (b) The cycling performances of MHCS electrodes at different current rates.

To further exploit the integrity of the MHCS electrode and electrochemical impedance changes before and after 200 cycles, *ex-situ* SEM analysis, elemental mapping and EIS measurement were performed on the cycled electrodes. The elemental mapping image of the MHCS electrode after cycling is shown in Figure S7a (Supplementary information). Sulfur is still confined in the interlayer spaces of multi-shelled hollow carbon nanospheres, and no sulfur can be observed on the outside of the multi-shelled hollow carbon nanospheres, indicating that the unique carbon architecture can effectively prevent the loss of sulfur and suppress the shuttle effect. Figure

S7b and S7c (Supplementary information) clearly distinguish the distribution of sulfur and carbon. The EDX spectrum in Figure S7d (Supplementary information) shows the elemental information. Even after long time cycling, the robust multi-shelled hollow carbon nanosphere-sulfur composites can maintain their structure and integrity. The electrochemical impedance spectra are presented in Figure 6a and the corresponding equivalent circuit is shown in Figure 6b. The impedance spectra, consisting of a depressed semicircle in the high frequency area and an oblique line in the medium frequency region, reflect the changes of impedances of the electrode before and after 200 cycles. Obviously, there are little

changes of the radius of two semicircles in the high frequency region, illustrating that the electrochemical impedances do not increase dramatically. This further demonstrates the robust properties and superior conductivity of multi-shelled hollow carbon nanospheres, and the stable cycling characteristics of multi-shelled hollow carbon nanosphere-sulfur composites.

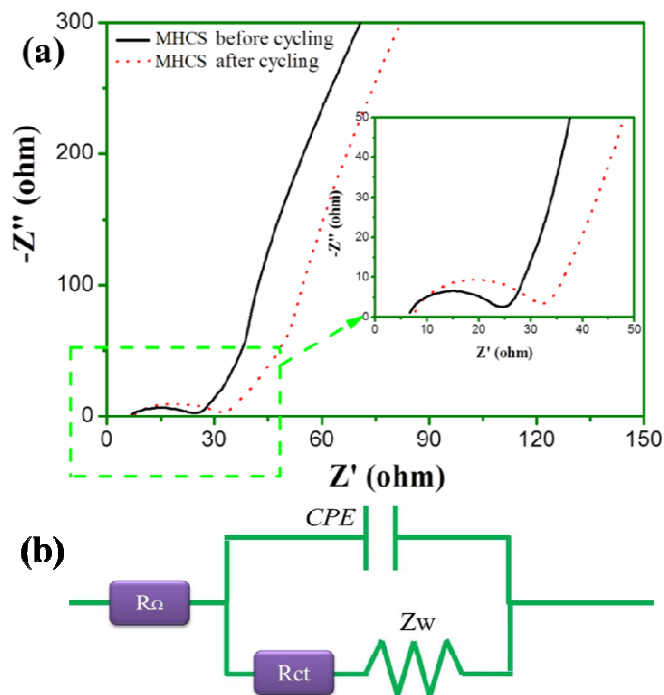


Figure 6. (a) Electrochemical impedance spectra of MHCS electrode before and after cycling. (b) The corresponding equivalent circuit (R_{Ω} : Ohm resistance; R_{ct} : Charge transfer resistance; Z_w : Warburg diffusion process; CPE: constant-phase element).

Based on the aforementioned analysis, the enhanced electrochemical performances of sulfur-rich MHCS composites can be ascribed to the rationally designed dual sulfur confining approach. The physical confinement of multi-shelled hollow carbon nanospheres and the chemical bonding force of the PVP polymer layer jointly restrain the sulfur loss during discharge/charge processes. Furthermore, the heat treatment of carbon nanospheres at high temperature can effectively enhance the conductivity of electrodes. The large inner voids and spaces in multiple carbon shells provide sufficient spaces to buffer the volume changes during charge/discharge. The high sulfur content in the composite electrodes can enhance both gravimetric and volumetric energy density. The electrolyte additive of LiNO_3 also assists in suppressing the shuttle effect originated from lithium polysulfide ions during both charge and discharge processes. TEM and elemental mapping confirmed that sulfur was fully encapsulated into intershell spaces and inner cores of multi-shelled hollow carbon nanospheres, which maintained the unique structure even after 200 cycles and exhibited the enhanced electrochemical performances.

Conclusions

In summary, the sulfur-rich (86 wt. %) MHCS composites were successfully synthesised by an aqueous emulsion approach and *in-situ* impregnation method. Multi-shelled hollow carbon nanospheres and PVP polymers were employed as a dual sulfur confining strategy. When applied as cathodes in lithium sulfur batteries, multi-shelled hollow carbon nanosphere-sulfur composites delivered a high specific capacity of 1350 mAh/g, and excellent cycling stability at the current density of 0.1C. Reversible curves from cyclic voltammogram curves validate successful suppression of shuttle effect. The electrode delivered 1003 mAh/g and 541 mAh/g at 1C and 5C in the initial cycle, respectively. After 200 cycles, specific capacities of the MHCS composites at 1C and 5C still maintained 846 mAh/g and 452 mAh/g with capacity retention ratios of 84% and 83.5%, respectively, which demonstrates enhanced cyclability and good capacity retentions.

Experimental

Preparation of resol precursors.

The resol precursor with a low molecular weight ($M_w < 500$) was made using a typical approach reported by Zhao's group.⁶¹ In a typical procedure, 4 g of phenol and 0.63 g of 20 wt.% NaOH aqueous solution were mixed under stirring at 40 ~ 43 °C in a flask for 10 min. Then, formalin (7 g, 37 wt.% formaldehyde) was added dropwise below 50 °C, and the reaction mixture was further stirred at 70 °C for 1h. After the mixture cooled to room temperature, the pH value was adjusted to neutral (around 7.0) by means of HCl solution. Then, water was evaporated in a vacuum oven at 50 °C overnight. Finally, the precursor was redissolved in ethanol before further use.

Synthesis of multi-shelled hollow carbon nanospheres.

Multi-shelled hollow mesoporous polymer-silica precursors and carbon nanospheres were prepared by the multi-constituent co-assembly method, assisted with Pluronic F127 ($M_w=12600$, poly(ethylene oxide)-*b*-poly(propylene oxide)-*b*-poly(ethylene oxide) (PEO-PPO-PEO), purchased from Sigma Aldrich) in an aqueous solution. The typical synthetic procedure can be described as follows: 0.5 g of Pluronic F127 was dissolved in a resol ethanolic solution (3.2 g) containing 4.0 mmol of phenol and 8.0 mmol of formaldehyde. Then, 3.75 g of ethanol mixed with 1.0 g of TMB was added to the aforementioned solution with strong stirring until forming a clear solution (marked as solution-1). Meanwhile, 1.2 g of Tetraethylorthosilicate (TEOS) was hydrolyzed in an aqueous solution of HCl (75 ml, 1M) at 40 °C for half an hour. Solution-1 was then added dropwise under continuous stirring, forming a lactic solution in a few seconds. After stirring for 12 h, the solution was transferred into an autoclave and maintained at 90 °C for 24 h. Then, lactic precipitates were obtained by filtration with copious water, and dried in air. After that, the precursors were calcined at 350 °C for 2h then 900 °C for 3h, with a heating rate of 1 °C/min for 3 h under N_2 , named as MHC-SiO₂. 200 mg of

calcined MHC-SiO₂ was treated with 50 ml of 2M NaOH solution, with stirring overnight, and then the multi-shelled hollow carbon nanospheres were obtained by filtration with copious de-ionized water and ethanol, and then dried at room temperature.

Preparation of multi-shelled hollow carbon nanosphere-sulfur composites:

50 mg as-synthesized hollow multi-shelled hollow carbon nanospheres were transferred in a mixed solution of sodium thiosulfate solution (3.2 mmol, 0.403 g dissolved into 50 ml de-ionized water and 10 ml ethanol) and sodium sulfide (6.4 mmol, 0.499 g) with strong stirring for 30 min. Hydrochloric acid (1M, 20 ml) solution was dropwise added to the dark suspension and stirred for 30 min. After this, 10 mg polyvinyl pyrrolidone (PVP) was added and maintained stirrings for 3 h. The suspension was then treated by pulsed sonication for 30 min (5s on and 5s off) in an ice bath using a Branson S-450D sonifier with a horn of 13 mm in diameter (40% amplitude). After that, the suspension was washed with de-ionized water and dried overnight in a vacuum oven at 80 °C. Finally, the composites were quickly placed in a preheated horizontal furnace (155 °C) with a flow of Ar (200 sccm) gas for 12 hrs, and then cooled to room temperature.

Structural and phase characterization.

The as-prepared hyperbranched carbon nanorods/sulfur composites were characterized by X-ray diffraction (Rigaku D/max-2550 V with Cu K α radiation) operated at 40 KV and 30 mA. Raman spectra were measured by a Renishaw inVia Raman spectrometer system (Gloucestershire, UK) equipped with a Leica DMLB microscope (Wetzlar, Germany) and a 17 mW at 633 nm Renishaw helium neon laser with 50% power. A thermogravimetric analyzer (TGA, SDT 2960) was used to measure the weight percentage of Si from RT to 800 °C in air. The morphologies and crystal structure of materials were analyzed by a field emission scanning electron microscope (JSM-6700F, 20 kV) and transmission electron microscope (TEM, JEOL JEM-2010F) equipped with an energy-dispersive X-ray spectroscopy (EDX).

Electrochemical measurements.

The working electrodes were made from 80 wt.% of active materials, 10 wt.% of the conductive agent (acetylene black), and 10 wt.% of the binder (Alginic acid sodium salt extracted from brown algae). The mixture was stirred by an adjustable high-speed electric agitator. The working electrodes were dried in a vacuum oven. The mass of each electrode on the aluminium current collector is around 3 mg. CR2032 coin cells were assembled in an argon-filled glove box (Mbraun, Unilab, Germany), in which both the moisture and oxygen contents were controlled to be less than 0.1 ppm. Lithium foil was used as the counter electrode. The electrolyte was 1 M lithium bis(trifluoromethanesulfonyl)imide (LiTFSI) and 1 wt.% lithium nitrate (LiNO₃) in 1,3-dioxolane and 1,2-dimethoxy-ethane (volume ratio 1:1). Electrochemical measurements were

performed using a LAND-CT2001C battery test system. The cells were discharged and charged galvanostatically in the fixed voltage range of 1.7–2.6 V, with a current density of 167.3 mA·g⁻¹ (0.1C). Higher current rates (0.5C, 1C and 5C) were also used to test the electrochemical performances. Cyclic voltammogram was measured on a CHI 660E electrochemical workstation, at a scan rate of 0.1 mV·S⁻¹.

Acknowledgements

We would thank the support from the Australian Research Council (ARC) and ARC Future Fellowship project as well as the China Scholarship Council.

Funding Sources

This project is financially supported by the Australian Research Council (ARC) through the ARC Discovery project (DP1093855), ARC Future Fellowship project (FT110100800) and partially supported from the China Scholarship Council (CSC, No. 2011689009).

Notes and references

Centre for Clean Energy Technology, School of Chemistry and Forensic Science, University of Technology, Sydney, NSW, 2007, Australia.

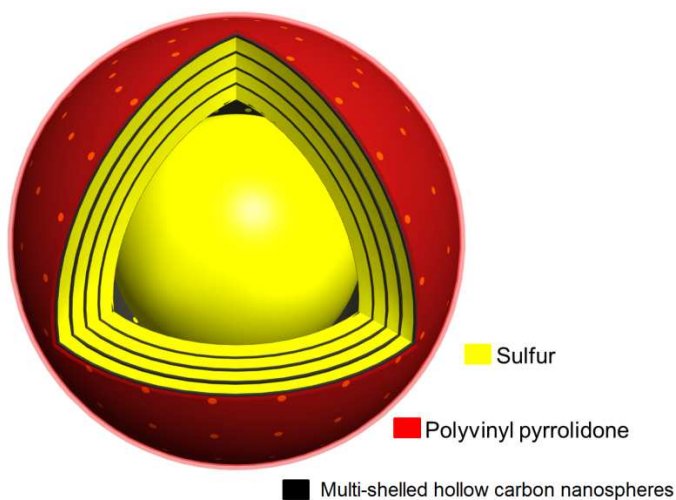
Electronic Supplementary Information (ESI) available: Nitrogen absorption and desorption of MHC-SiO₂, MHC, and MHCS composite, SEM images of pure sulphur particles, elemental mapping of MHCS composites, discharge/charge profile of pure sulfur, XRD patterns, Raman spectra, elemental line scan and energy dispersive X-ray spectrum of MHCS composite are presented in supplementary information. See DOI: 10.1039/b000000x/

Reference

1. M. Armand and J. M. Tarascon, *Nature*, 2008, **451**,652-657.
2. G. BrucePeter, A. FreunbergerStefan, J. HardwickLaurence and M. TarasconJean, *Nat. Mater.*, 2012, **11**,172-172.
3. C. K. Chan, H. Peng, G. Liu, K. McIlwrath, X. F. Zhang, R. A. Huggins and Y. Cui, *Nat. Nanotechnol.*, 2008, **3**,31-35.
4. N. Liu, H. Wu, M. T. McDowell, Y. Yao, C. Wang and Y. Cui, *Nano Lett.*, 2012, **12**,3315-3321.
5. S. Chen, P. Bao and G. Wang, *Nano Energy*, 2013, **2**,425-434.
6. S. Chen, P. Chen, M. Wu, D. Pan and Y. Wang, *Electrochem Commun*, 2010, **12**,1302-1306.
7. Z.-S. Wu, G. Zhou, L.-C. Yin, W. Ren, F. Li and H.-M. Cheng, *Nano Energy*, 2012, **1**,107-131.
8. S. Chen, P. Bao, X. Huang, B. Sun and G. Wang, *Nano Res.*, 2014, **7**,85-94.
9. R. Yi, F. Dai, M. L. Gordin, H. Sohn and D. Wang, *Adv. Energy Mater.*, 2013, **3**,1507-1515.
10. W. Li, G. Zheng, Y. Yang, Z. W. Seh, N. Liu and Y. Cui, *Proc. Natl. Acad. Sci.*, 2013, **110**,7148-7153.
11. Y. Yang, G. Zheng and Y. Cui, *Chem. Soc. Rev.*, 2013, **42**,3018-3032.
12. X. Ji, K. T. Lee and L. F. Nazar, *Nat. Mater.*, 2009, **8**,500-506.
13. Y. Yang, G. Zheng and Y. Cui, *Energ. Environ. Sci.*, 2013, **6**,1552-1558.
14. J. Gao and H. D. Abruña, *J. Phys. Chem. Lett.*, 2014, **5**,882-885.
15. L. Wang, T. Zhang, S. Yang, F. Cheng, J. Liang and J. Chen, *J. Energ. Chem.*, 2013, **22**,72-77.

16. L. Xiao, Y. Cao, J. Xiao, B. Schwenzer, M. H. Engelhard, L. V. Saraf, Z. Nie, G. J. Exarhos and J. Liu, *Adv. Mater.*, 2012, **24**, 1176-1181.
17. G.-C. Li, G.-R. Li, S.-H. Ye and X.-P. Gao, *Adv. Energy Mater.*, 2012, **2**, 1238-1245.
18. R. Chen, T. Zhao, J. Lu, F. Wu, L. Li, J. Chen, G. Tan, Y. Ye and K. Amine, *Nano Lett.*, 2013, **13**, 4642-4649.
19. B. Wang, K. Li, D. Su, H. Ahn and G. Wang, *Chem. Asian J.*, 2012, **7**, 1637-1643.
20. G. Zheng, Y. Yang, J. J. Cha, S. S. Hong and Y. Cui, *Nano Lett.*, 2011, **11**, 4462-4467.
21. N. Jayaprakash, J. Shen, S. S. Moganty, A. Corona and L. A. Archer, *Angew. Chem. Int. Ed.*, 2011, **50**, 5904-5908.
22. C. B. Bucur, J. Muldoon, A. Lita, J. B. Schlenoff, R. A. Ghostine, S. Dietz and G. Allred, *Energ. Environ. Sci.*, 2013, **6**, 3286-3290.
23. L. Yin, J. Wang, F. Lin, J. Yang and Y. Nuli, *Energ. Environ. Sci.*, 2012, **5**, 6966-6972.
24. Y. Cao, X. Li, I. A. Aksay, J. Lemmon, Z. Nie, Z. Yang and J. Liu, *Phys. Chem. Chem. Phys.*, 2011, **13**, 7660-7665.
25. J.-Q. Huang, X.-F. Liu, Q. Zhang, C.-M. Chen, M.-Q. Zhao, S.-M. Zhang, W. Zhu, W.-Z. Qian and F. Wei, *Nano Energy*, 2013, **2**, 314-321.
26. J.-Q. Huang, Q. Zhang, S.-M. Zhang, X.-F. Liu, W. Zhu, W.-Z. Qian and F. Wei, *Carbon*, 2013, **58**, 99-106.
27. F. Wu, J. Chen, L. Li, T. Zhao, Z. Liu and R. Chen, *ChemSusChem*, 2013, **6**, 1438-1444.
28. K. Li, B. Wang, D. Su, J. Park, H. Ahn and G. Wang, *J Power Sources*, 2012, **202**, 389-393.
29. L. Xiao, Y. Cao, J. Xiao, B. Schwenzer, M. H. Engelhard, L. V. Saraf, Z. Nie, G. J. Exarhos and J. Liu, *J. Mater. Chem. A*, 2013, **1**, 9517-9526.
30. M.-K. Song, Y. Zhang and E. J. Cairns, *Nano Lett.*, 2013, **13**, 5891-5899.
31. C. Zhang, H. B. Wu, C. Yuan, Z. Guo and X. W. Lou, *Angew. Chem. Int. Ed.*, 2012, **51**, 9592-9595.
32. K. Zhang, Q. Zhao, Z. Tao and J. Chen, *Nano Res.*, 2013, **6**, 38-46.
33. B. Zhang, X. Qin, G. R. Li and X. P. Gao, *Energ. Environ. Sci.*, 2010, **3**, 1531-1537.
34. Y.-S. Su and A. Manthiram, *Nat. Commun.*, 2012, **3**, 1166.
35. C. Zu and A. Manthiram, *Adv. Energy Mater.*, 2013, **3**, 1008-1012.
36. G. Zhou, S. Pei, L. Li, D.-W. Wang, S. Wang, K. Huang, L.-C. Yin, F. Li and H.-M. Cheng, *Adv. Mater.*, 2014, **26**, 625-631.
37. G. Yu, X. Xie, L. Pan, Z. Bao and Y. Cui, *Nano Energy*, 2013, **2**, 213-234.
38. S. Dorfler, M. Hagen, H. Althues, J. Tubke, S. Kaskel and M. J. Hoffmann, *Chem. Commun.*, 2012, **48**, 4097-4099.
39. S. Moon, Y. H. Jung, W. K. Jung, D. S. Jung, J. W. Choi and D. K. Kim, *Adv. Mater.*, 2013, **25**, 6547-6553.
40. T. P. McNicholas, L. Ding, D. Yuan and J. Liu, *Nano Lett.*, 2009, **9**, 3646-3650.
41. G. Zheng, Q. Zhang, J. J. Cha, Y. Yang, W. Li, Z. W. Seh and Y. Cui, *Nano Lett.*, 2013, **13**, 1265-1270.
42. F. Sun, J. Wang, H. Chen, W. Qiao, L. Ling and D. Long, *Sci. Rep.*, 2013, **3**, 2823-2831.
43. H. Chen, W. Dong, J. Ge, C. Wang, X. Wu, W. Lu and L. Chen, *Sci. Rep.*, 2013, **3**.
44. G. Xu, B. Ding, P. Nie, L. Shen, J. Wang and X. Zhang, *Chem. Eur. J.*, 2013, **19**, 12306-12312.
45. W. Li, Q. Zhang, G. Zheng, Z. W. Seh, H. Yao and Y. Cui, *Nano Lett.*, 2013, **13**, 5534-5540.
46. H. Wang, Y. Yang, Y. Liang, J. T. Robinson, Y. Li, A. Jackson, Y. Cui and H. Dai, *Nano Lett.*, 2011, **11**, 2644-2647.
47. R. Demir-Cakan, M. Morcrette, F. Nouar, C. Davoisne, T. Devic, D. Gonbeau, R. Dominko, C. Serre, G. Férey and J.-M. Tarascon, *J. Am. Chem. Soc.*, 2011, **133**, 16154-16160.
48. X. Ji, S. Evers, R. Black and L. F. Nazar, *Nat. Commun.*, 2011, **2**, 325.
49. Y. Yang, G. Yu, J. J. Cha, H. Wu, M. Vosgueritchian, Y. Yao, Z. Bao and Y. Cui, *ACS Nano*, 2011, **5**, 9187-9193.
50. W. Zhou, H. Chen, Y. Yu, D. Wang, Z. Cui, F. J. DiSalvo and H. D. Abruña, *ACS Nano*, 2013, **7**, 8801-8808.
51. G. He, S. Evers, X. Liang, M. Cuisinier, A. Garsuch and L. F. Nazar, *ACS Nano*, 2013, **7**, 10920-10930.
52. C. Huang, J. Xiao, Y. Shao, J. Zheng, W. D. Bennett, D. Lu, L. V. Saraf, M. Engelhard, L. Ji, J. Zhang, X. Li, G. L. Graff and J. Liu, *Nat. Commun.*, 2014, **5**.
53. Z. Dong, X. Lai, J. E. Halpert, N. Yang, L. Yi, J. Zhai, D. Wang, Z. Tang and L. Jiang, *Adv. Mater.*, 2012, **24**, 1046-1049.
54. J. Wang, N. Yang, H. Tang, Z. Dong, Q. Jin, M. Yang, D. Kisailus, H. Zhao, Z. Tang and D. Wang, *Angew. Chem. Int. Ed.*, 2013, **52**, 6417-6420.
55. S. Xu, C. M. Hessel, H. Ren, R. Yu, Q. Jin, M. Yang, H. Zhao and D. Wang, *Energ. Environ. Sci.*, 2014, **7**, 632-637.
56. J. Du, J. Qi, D. Wang and Z. Tang, *Energ. Environ. Sci.*, 2012, **5**, 6914-6918.
57. X. Lai, J. E. Halpert and D. Wang, *Energ. Environ. Sci.*, 2012, **5**, 5604-5618.
58. J. Qi, K. Zhao, G. Li, Y. Gao, H. Zhao, R. Yu and Z. Tang, *Nanoscale*, 2014, **6**, 4072-4077.
59. F. Su, C. K. Poh, J. S. Chen, G. Xu, D. Wang, Q. Li, J. Lin and X. W. Lou, *Energ. Environ. Sci.*, 2011, **4**, 717-724.
60. L. Yi, Y. Liu, N. Yang, Z. Tang, H. Zhao, G. Ma, Z. Su and D. Wang, *Energy & Environmental Science*, 2013, **6**, 835-840.
61. D. Gu, H. Bongard, Y. Deng, D. Feng, Z. Wu, Y. Fang, J. Mao, B. Tu, F. Schüth and D. Zhao, *Adv. Mater.*, 2010, **22**, 833-837.
62. G. Zhou, L.-C. Yin, D.-W. Wang, L. Li, S. Pei, I. R. Gentle, F. Li and H.-M. Cheng, *ACS Nano*, 2013, **7**, 5367-5375.
63. Z. Lin, Z. Liu, N. J. Dudney and C. Liang, *ACS Nano*, 2013, **7**, 2829-2833.
64. C. Zhang, W. Lv, W. Zhang, X. Zheng, M.-B. Wu, W. Wei, Y. Tao, Z. Li and Q.-H. Yang, *Adv. Energy Mater.*, 2013, DOI: 10.1002/aenm.201301565, n/a-n/a.
65. S. Chen, X. Huang, H. Liu, B. Sun, W. Yeoh, K. Li, J. Zhang and G. Wang, *Adv. Energy Mater.*, 2014, DOI: 10.1002/aenm.201301761, n/a-n/a.
66. S. Zheng, Y. Chen, Y. Xu, F. Yi, Y. Zhu, Y. Liu, J. Yang and C. Wang, *ACS Nano*, 2013, **7**, 10995-11003.
67. S. Wei, H. Zhang, Y. Huang, W. Wang, Y. Xia and Z. Yu, *Energ. Environ. Sci.*, 2011, **4**, 736-740.
68. J. Schuster, G. He, B. Mandlmeier, T. Yim, K. T. Lee, T. Bein and L. F. Nazar, *Angew. Chem. Int. Ed.*, 2012, **51**, 3591-3595.
69. Z. Li, L. Yuan, Z. Yi, Y. Liu, Y. Xin, Z. Zhang and Y. Huang, *Nanoscale*, 2014, **6**, 1653-1660.

Table of Content (TOC)



Multi-shelled hollow carbon nanospheres with a high specific surface area of $1050 \text{ m}^2/\text{g}$ were prepared by an aqueous emulsion approach, which achieved a high percentage of sulfur loading (86 wt. %). When applied as cathodes in lithium-sulfur batteries, the sulfur composites delivered a high specific capacity of 1350 mAh/g at the current rate of 0.1C (167.3 mA/g), a significantly enhanced cyclability and high rate performances.